ABSORPTION PHENOMENA AND A PROBABLE BLAST WAVE IN THE 13 JULY 2004 ERUPTIVE EVENT

V. V. GRECHNEV[1], A. M. URALOV[1], V. A. SLEMZIN[2],
I. M. CHERTOK[3], I. V. KUZMENKO[4], K. SHIBASAKI[5]
[1] *Institute of Solar-Terrestrial Physics SB RAS, Lermontov St. 126, Irkutsk 664033, Russia* (grechnev@iszf.irk.ru)
[2] *P.N. Lebedev Physical Institute, Lenisky Pr., 53, Moscow, 119991, Russia*
[3] *Pushkov Institute of Terrestrial Magnetism, Ionosphere and Radio Wave Propagation (IZMIRAN), Troitsk, Moscow Region, 142190 Russia*
[4] *Ussuriysk Astrophysical Observatory, Solnechnaya St. 21, Primorsky Krai, Gornotaezhnoe 692533, Russia*
[5] *Nobeyama Radio Observatory, Minamimaki, Minamisaku, Nagano 384-1305, Japan*

Received ; accepted

Abstract. We present a case study of the 13 July 2004 solar event, in which disturbances caused by eruption of a small filament from a compact active region embraced a quarter of the visible solar surface. Remarkable are absorption phenomena, which showed up in the SOHO/EIT 304 Å channel; they were also observed in the EIT 195 Å channel, in the Hα line, and even in total radio flux records. Quantitative evaluations from different observations provide close estimates of the ejected mass, $\sim 3 \cdot 10^{15}$ g. Coronal and Moreton waves observed in this event were kinematically close and both decelerated in accordance with an expected motion of a coronal blast shock associated with the eruption. Multi-spectral data allow to reconstruct a picture of the whole event initiated by the eruption of the filament. The ejected structure disintegrated, and some its part fell back onto the Sun, while another part flew away and produced a decelerating CME, which did not resemble a classical three-component structure. The falling material was responsible for the observed large-scale absorption phenomena, in particular, shallow moving dimmings observed at 195 Å. Deep, long-lived dimmings observed in this band were due to plasma density decrease in coronal structures.

Keywords: Sun: corona, Sun: coronal mass ejections (CMEs), Sun: filaments, Sun: radio radiation, Sun: UV radiation

1. Introduction

Some major flares and coronal mass ejections (CMEs) are accompanied by large-scale features like Moreton waves, transient coronal brightenings (usually termed 'EIT waves') moving over distances comparable with the solar radius, and temporary depressions of soft X-ray (SXR) and extreme-ultraviolet (EUV) emissions (termed dimmings) appearing near the eruption center and far from it. They have been observed with the Extreme-ultraviolet Imaging Telescope (EIT; Delaboudinière *et al.*, 1995) on SOHO, Transition Region and Coronal Explorer (TRACE; Handy *et al.*, 1999), and other telescopes. Nevertheless, nature of all these phenomena is still controversial.

Moreton waves are sometimes observed in the Hα line (Moreton, 1960) and, more recently, in the He I 10830 Å line (e.g., Vršnak *et al.*, 2002; Gilbert *et al.*, 2004a). Uchida (1968) proposed them to be due to coronal disturbances. Balasubramaniam, Pevtsov, and Neidig (2007) also argued their coronal nature. However, Moreton waves run faster (400–2000 km s^{-1}) than 'EIT waves' (< 800 km s^{-1}, typically about 250 km s^{-1}). Nevertheless, Warmuth *et al.* (2001, 2004a, 2004b, 2005) found their kinematical closeness and proposed that both chromospheric and coronal signatures of the waves could be created by a single decelerating disturbance, e.g., a blast shock (see also Hudson and Warmuth, 2004). Gilbert *et al.* (2004a, 2004b) found 'EIT waves' to be co-spatial with their chromospheric counterparts in He I.

Some observations favor wave nature of 'EIT waves' (e.g., Ballai, Erdélyi, and Pintér, 2005). A few moving bright features were interpreted as CME frontal magnetic structures (e.g., Dere *et al.*, 1997; Uralov, Grechnev, and Hudson, 2005). Several authors try to explain both 'EIT waves' and dimmings by a common scenario. Delannée and Aulanier (1999) proposed 'EIT waves' to be a running boundary of successively opening magnetic structures ahead of an expanding dimming area, from which plasmas evacuate. A reconnection-based scenario of Attrill *et al.* (2007) also relates 'EIT waves' with moving dimmings. However, dimmings are not commonly associated with 'EIT waves' (e.g., Chertok and Grechnev, 2005b; Grechnev *et al.*, 2005).

Trying to reconcile contradictory views, Zhukov and Auchère (2004) proposed 'bimodality' of 'EIT waves', i.e., that they represent both a wave-like component and an eruptive one. Simulations of Chen *et al.* (2002, 2005) confirmed a possibility of two types of wave phenomena in the corona during an eruption, one according to the scenario of Delannée and Aulanier (1999), and a fast coronal counterpart of the Moreton wave ahead.

Dimmings develop from $\sim$10 minutes up to several hours, live up to two days (Hudson and Webb, 1997), and reach -80% (Chertok and Grechnev, 2003a, 2005b). Having once appeared in some region, deep, long-lived dimmings do not leave it (Chertok and Grechnev, 2005b; Grechnev et al., 2005). Their main interpretation is plasma density depletion due to its evacuation from previously closed coronal structures (see also Harra and Sterling, 2001). Such dimmings are related with active regions and large-scale magnetic fields (Chertok and Grechnev, 2005b; Slemzin, Kuzin, and Bogachev, 2005; Slemzin, Grechnev, and Kuzin, 2006; Zhang *et al.*, 2007).

Some moving shallow darkenings seem to accompany 'EIT waves' in their expansion (see, e.g., Zhukov and Auchère, 2004; Grechnev *et al.* 2005). They can have the same wave-like nature as such 'EIT waves'. Another kind of short-lived, moving darkenings could be due to occultation of the background emission by absorbing material of ejecta. Such phenomena have been observed in EUV images produced with EIT in the 195 Å (Fe XII) band and TRACE in the 195 Å and 173 Å (Fe IX) coronal bands. In particular, darkenings sometimes observed with EIT in the 304 Å band (mainly He II, 20 000–80 000 K) without counterparts in coronal bands (see, e.g., Chertok and Grechnev, 2003b; Slemzin *et al.*, 2004; Grechnev *et al.*, 2005) are expected to be certainly due to absorption in material of an ejected filament (Delaboudinière, 2005).

Such a phenomenon was observed with the CORONAS-F/SPIRIT EUV telescope (Zhitnik *et al.*, 2002) in a major event of November 18, 2003 (Slemzin *et al.*, 2004; Grechnev *et al.*, 2005). A dark feature as large as the solar radius was observed at 304 Å band only to move during 1.5 hr across the Sun with a sky-plane speed of $\simeq 200\,\mathrm{km\,s^{-1}}$. Thus, increasing observational material suggests that different kinds of both 'EIT waves' and dimmings probably exist (as also Warmuth *et al.* (2001) proposed).

'Negative bursts' are believed to be often also due to absorption (e.g., Covington and Dodson, 1953), but in the radio domain (other reasons are also possible; e.g., Sawyer, 1977; Maksimov and Nefedyev, 1991). Since opacity of an absorber to radio emission depends on frequency and plasma parameters, multi-frequency observations of such bursts give an opportunity of quantitative diagnostics of ejecta. It seems to be promising to juxtapose observations of an event, in which absorption occurred both in EUV and radio ranges.

This paper addresses the 13 July 2004 solar event, in which a multi-component eruption, CME, Moreton and coronal waves, large-scale EUV absorption phenomena and long-lived dimmings as well as a 'negative radio burst' were well observed simultaneously in different ranges. The event included an impulsive M6.7 flare (00:09–00:23, all times hereafter are UT) in active region 10646 (N13 W46) and a CME with a central position angle of 294° observed from 00:54 onwards with the Large-Angle Spectrometric Coronagraph (LASCO; Brueckner *et al.*, 1995) on SOHO. EIT observed large-scale disturbances in the 195 Å band, in particular, a faint oval front at 00:24. According to Solar Geophysical Data[1], a type II burst at 00:16–00:43 was reported by a few observatories. At 01:19, a large-scale darkening was observed in a single frame of EIT at 304 Å. During this event, a strong impulsive radio burst was recorded at 1–80 GHz with a long post-burst decrease of the radio emission. This 'negative burst' was revealed in total flux records of Ussuriysk Astrophysical Observatory (UAFO, 2.8 GHz), Nobeyama Radio Polarimeters (NoRP; Nakajima *et al.*, 1985; Torii *et al.*, 1979), and Learmonth Observatory. The event was also recorded in the Hα central line at Big Bear (BBSO) and Mauna Loa (MLSO) Solar Observatories, in the He I line in MLSO, and in the TRACE 173 Å channel. The Nobeyama Radioheliograph (NoRH; Nakajima *et al.*, 1994) observed some fragments of the ejecta at 17 GHz.

[1] http://sgd.ngdc.noaa.gov/sgd/jsp/solarindex.jsp

Using multi-spectral data, we study this event and reconstruct a picture of the eruption. The role of gravity was substantial; the ejecta disintegrated, and one its part fell back onto the Sun, while another part flew away. The dispersed material was responsible for the observed large-scale absorption phenomena. Estimations of masses are performed for both these parts by means of different methods that quantitatively confirm the inferred picture.

The event was initiated by an explosive filament eruption, which likely produced a blast wave. The measured kinematical plots of the wave and ejected fragments are compared with analytical expressions, which provide satisfactory fits with results of measurements. Some other aspects of this event concerning radio bursts, pulsations and their association with flare, ejecta, and shocks are addressed by Pohjolainen, Hori, and Sakurai (2007).

We start our consideration in Section 2 with observational data. In Section 3, we address absorption in different emissions and estimate the mass of the ejecta. In Section 4, we discuss kinematical characteristics of the observed phenomena and compare them with theoretical expectations. In Section 5, we discuss results of our analysis, the inferred overall picture of the event, and nature of 'EIT waves' and dimmings in this event. We then briefly summarize our findings and their implications in Section 5.4.

2. Observations

2.1. Filament Eruption, Moreton Wave, and Surge in Hα Images

Observations of the 13 July 2004 event in the Hα center line have been carried out in Big Bear (BBSO) and Mauna Loa (MLSO) Solar Observatories. No Hα flare was reported for this event, but images obtained in both observatories show it and related eruptive activities. Figure 1 presents Hα images obtained in BBSO (courtesy of V. Yurchyshyn). Before the eruption, the active region contained a system of rather small filaments. Filament 1–2 starts to rise at $\sim$00:02:30 with an acceleration of its top $\simeq 16\,\mathrm{m\,s^{-2}}$, which reaches 7000 km at 00:13:25 with a speed of $\gtrsim 22\,\mathrm{km\,s^{-1}}$ (according to the 2$^{\mathrm{nd}}$ order polynomial fit, which matches measurements)[2]. It erupts between 00:13:25 and 00:15:25. A fast Moreton wave propagates from the eruption site north/northeast (Figure 2). At about the onset of the Moreton wave, surge 1–3 from the western end of the filament starts to grow north/northwest with an average speed $\simeq 270\,\mathrm{km\,s^{-1}}$ at 00:18–00:23. By $\sim$00:21, the surge is accompanied by a parallel bright jet (frame b). After the pass of the Moreton wave, emitting loop-like structures form northerly of the eastern end 2 of the filament. At 00:17–00:18, a surge from this end of the filament appears and takes a V-like shape by 00:26 (frame c).

[2] All measurements are related to the sky plane

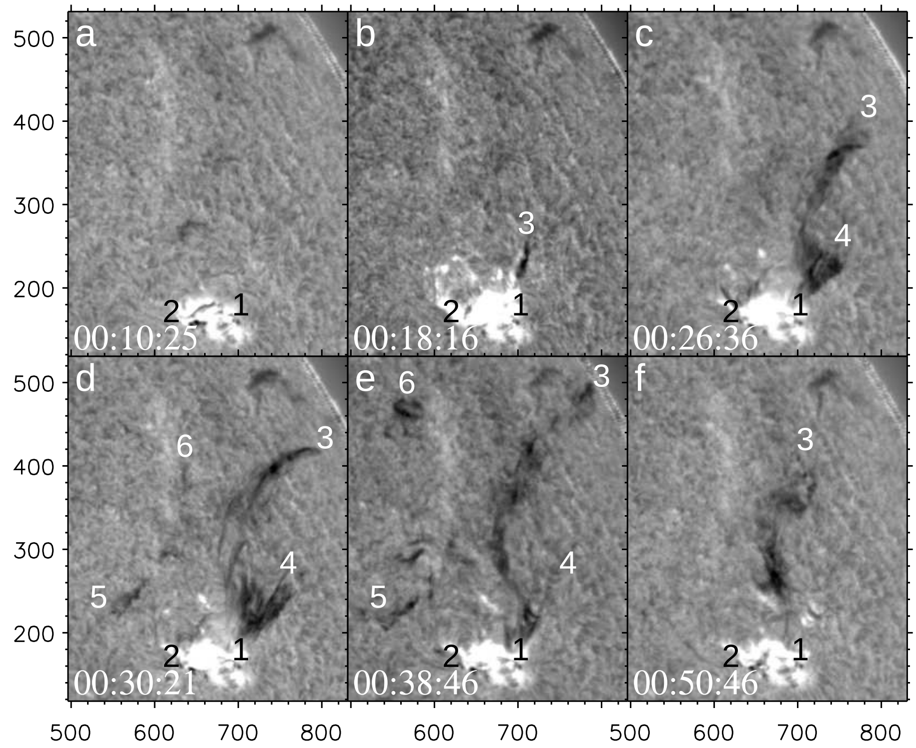

Figure 1. Hα images produced in the Big Bear Solar Observatory. Limb darkening removed. Labels denote features discussed in the text. Axes show arc seconds from the solar disk center.

The western surge 1–3 consisting of a multitude of thin, likely twisted threads intensively develops during this interval. After about 00:22, it starts to bifurcate into the northwest (1–4) and north (1–3) branches. Branch 1–4 rises up to its maximum height of $\simeq 90$ Mm at about 00:30 and then mainly disappears. Branch 1–3 rises (moves north) with an average speed $\simeq 270\,\mathrm{km\,s^{-1}}$ (00:18–00:29) and simultaneously moves slightly east; new threads appear herewith. Along with fragments of the filament emanating from the eastern vicinity 2 of the main filament(s) and a newly appeared, remote dark feature 5, to 00:30 they form a large-scale filamentary structure. Its components occupy a significant area 1–4–3–6–5–2 in frame (d). Then this area continues to expand north and east, especially, due to the northern part of branch 3 and fragment 6 (frame e). Feature 6 moves roughly toward the North Pole with a speed $\simeq 155\,\mathrm{km\,s^{-1}}$ (00:31–00:53). As MLSO HeI 10830 Å images show, the disturbance probably associated with this moving feature reaches vicinities of the northern polar coronal hole at $\simeq$01:20. After 00:50, the Hα surge partially falls back and becomes fainter. This is due to ei-

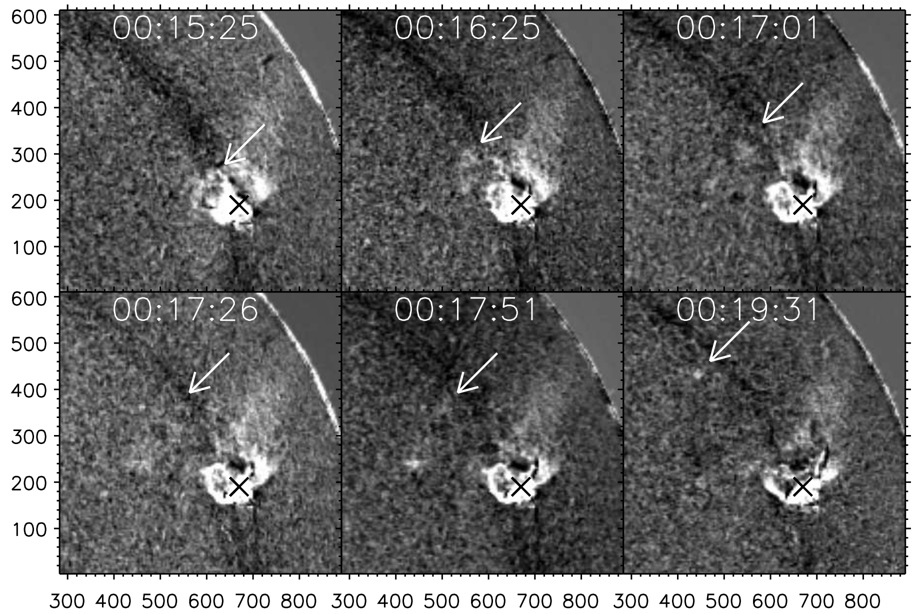

Figure 2. Moreton wave (the front indicated by the arrows) in BBSO Hα images with subtracted average image. The dark wide ring is an artifact (a 'trace' of the active region that appeared in a toroidal Fourier transform in the course of background subtraction). All images are displayed nonlinearly to emphasize the wave. The cross marks the eruption center. Axes show arc seconds from the solar disk center.

ther spreading out its components that decreases its optical depth, or their increasing line-of-sight velocities that results in the Doppler brightening. Throughout the almost entire development of the surge, many threads and fragments keep their connection with the position of the initial filament(s) 1–2, and their bases rest on its (their) vicinities.

From Hα data we conclude that a filament eruption resulted in formation of some large-scale 'dome' of filament's threads and fragments to cover in several tens of minutes a significant northwest part of the Sun.

2.2. High-Resolution TRACE 173 Å Images of the Eruption

TRACE observed the event starting from 00:07:27 in the 173 Å channel mainly with intervals from 20 to 70 s, except for the gap of 00:21–00:48. Figure 3 presents several images of the eruption region, which TRACE permits to discern like a magnifier. One can see in pre-eruption TRACE images a dark filament(s) and a bright rope along it as well as the northern and southern loop systems surrounding the region.

Four enlarged images (this area is outlined in panels *e* and *f* by dotted frames) in panels *a*–*d* show two closely located side-by-side filaments to

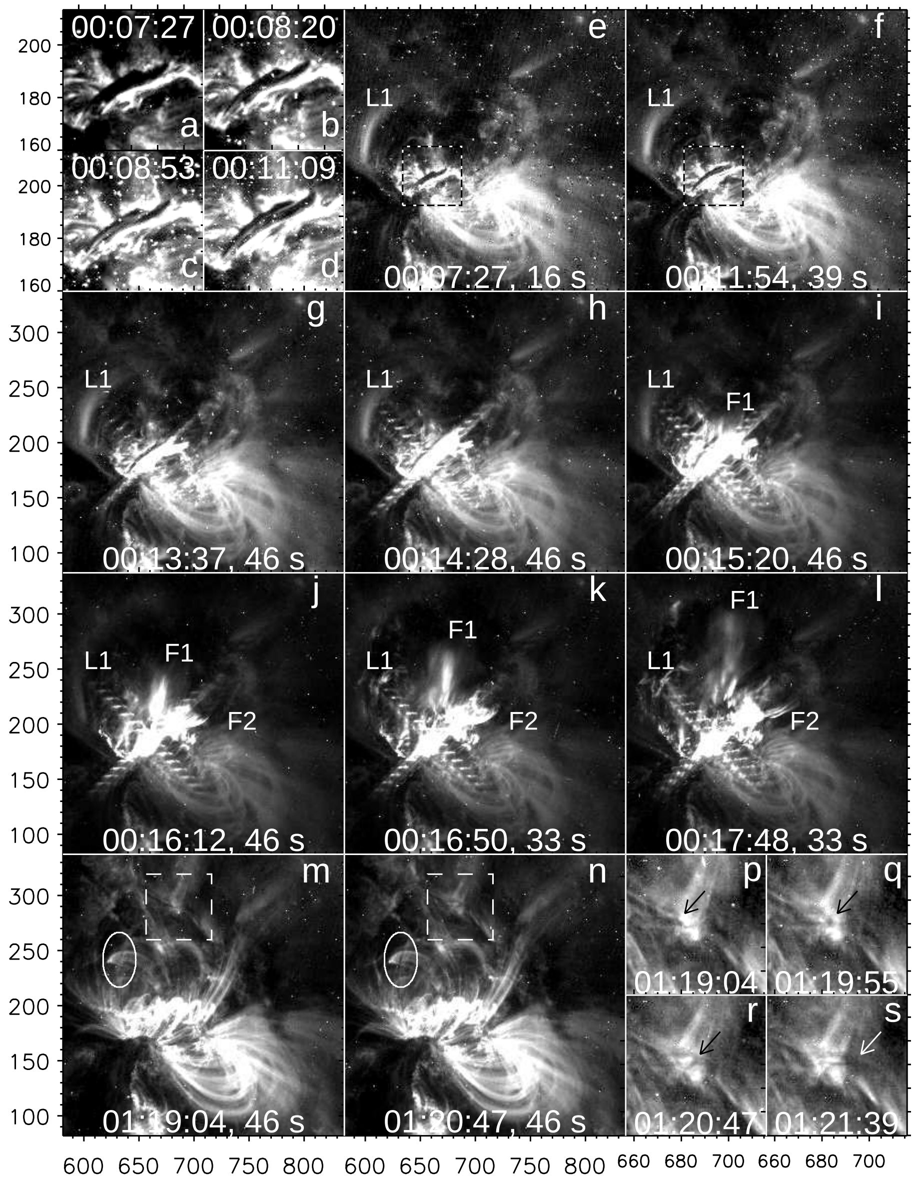

Figure 3. TRACE 173 Å images of the eruption: *a–l*, the early stage; *m–s*, the late stage. Insets *a–d* show enlarged images of filaments outlined in panels *e* and *f* by dotted frames. Labels *L1* in panels *e–l* mark an initial position of an erupting loop. Labels *F1* and *F2* mark bright jet-like moving features (position of label *F2* is fixed). Insets *p–s* show enlarged areas outlined in panels *m* and *n* by dashed frames, in which a flow of absorbing material is indicated by the arrows. Another flowing absorbing feature is outlined by an ellipse in panels *m* and *n*. Observation and exposure times are specified in frames *e–n*. All images are nonlinearly displayed. Axes show arc seconds from the solar disk center.

'merge' and start to expand up. The expansion of the combined filament is visible in subsequent frames *e–l*; in the course of its rise, the filament becomes semi-transparent, and its parts become detectable (*j*,*k*). Loop *L1* expands in frames *i–k* and disappears by 00:18 (*l*). A flare starts beneath the filaments by 00:13:37. In frame *i*, bright, apparently diffuse material appears above the whole combined filament, and later, in frames *j–l*, its brightest part appears as a jet-like feature *F1* moving north (up). Another, the slower bright jet-like feature *F2* moves west-northwest in frames *j–l*. Crossly dark/bright patterns are due to interference on the CCD matrix.

The speed of feature *F1* is 400–500 $\mathrm{km\,s^{-1}}$, which was acquired in ≤ 2 min (acceleration $\geq 8\ \mathrm{km\,s^{-2}}$). With this speed and exposure times t_{exp} shown in frames, apparent extents of this feature are $(400-500)\cdot t_{\mathrm{exp}} R_{\odot}^{\mathrm{arcsec}}/R_{\odot}^{\mathrm{km}} \simeq (18'' - 31'')$. Thus, a reason for its jet-like appearance is blurring due to its displacement during the exposure. The same reason explains the semi-transparent appearance of the filaments. They remain dark in all frames, where they are visible (by 00:17:48). Their speed is less by a factor of ~ 2.

Therefore, we conclude that the eruption occurs between 00:14:28 and 00:15:20. The eruptive filament remains cool. It is surrounded by a hotter envelope with probable temperatures of 0.3–1.6 MK (from the temperature sensitivity range of the TRACE 173 Å channel; Handy *et al.*, 1999).

In later images after the gap in observations, a post-eruptive arcade is visible. Interesting are dark moving flows occulting brighter structures behind them. Examples of the flows are outlined by ovals and dashed frames in *m*, *n* (enlarged images of the same area are shown in insets *p–s*, where the flow is indicated by the arrows) and by an ellipse. These flows represent moving absorbing (probably cool) material likely directed along magnetic field lines. Note also shrinkage of loops that we do not discuss in this paper.

The eruption destroyed the northern loop system. Loop *L1* erupted and not reappeared. The southern loop system remained almost unchanged. The eruption looks like a 'directional explosion' pointed northwards.

2.3. Coronal Disturbances in SOHO/EIT 195 Å Images

EIT carried out the routine *CME Watch* program, during which the 195 Å images are produced every 12 min. Figure 4 shows a pre-event (*a*) and a late-stage (*e*) images along with six fixed-base differences b–d and f–h with preliminary compensated solar rotation (see Chertok and Grechnev, 2005b). Figure 5 provides supplementary information about large-scale faint disturbances, which are easier observable in running-difference images.

The eruption caused significant disturbances in the corona, both brightening and darkening, which cover a huge area of the solar disk, even exceeding its NW quadrant. A nearly perfect oval brightening is seen at 00:24 Figure 4c and Figure 5b. It is not uniform in brightness and faint, mainly 5–15

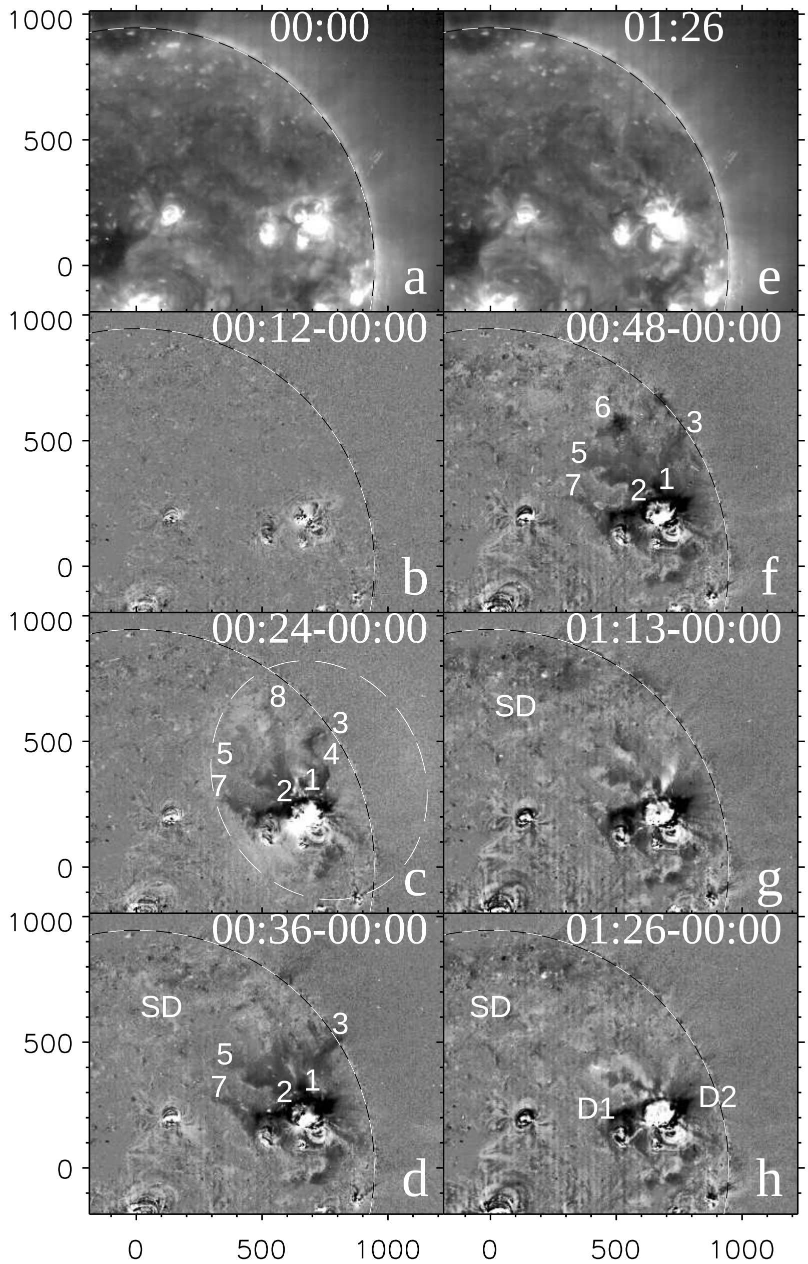

Figure 4. SOHO/EIT 195 Å images of the event. (a) Pre-event image, (e) later-stage image. Fixed-base (00:40 UT) differences (b–d and f–h) show large-scale coronal disturbances. Nonlinear display is applied to emphasize them. Dashed black-white circles denotes the solar limb. Dashed white oval traces the aureole discussed in the text. Labels 1–8 denote darkenings; D1 and D2, long-lived dimmings.

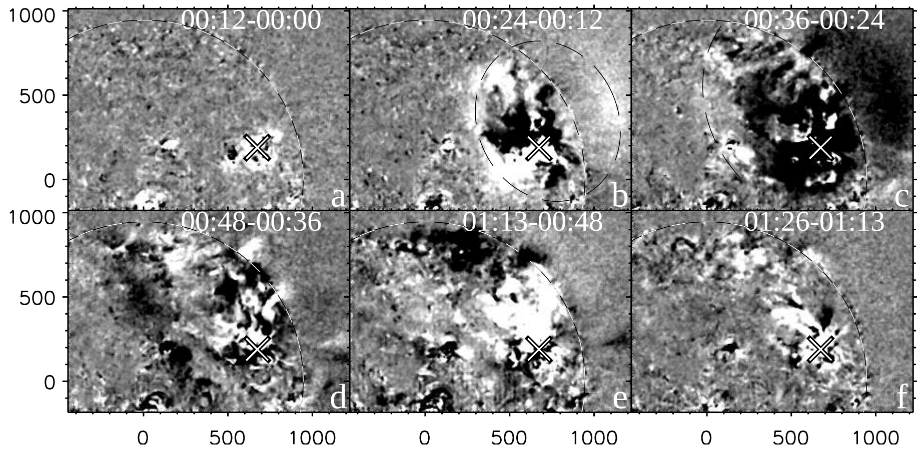

Figure 5. Large-scale disturbances in the NW quadrant visible in running-difference SOHO/EIT 195 Å images (nonlinearly displayed). Dashed circle denotes the solar limb. The cross marks the eruption center.

counts/pixel, while the brightness of quiet Sun's regions is about 40–50 and 5–21 in coronal holes. Three wide brightening sectors directed east-southeast, northeast, and west-southwest spread toward the oval from inside. The oval expands; its next position detectable on the solar disk is denoted by a dashed arc in Figure 5c (00:36).

Darkening areas are also pronounced in panels c, d, f–h of Figure 4. Some of them, mostly short-lived those, coincide with dark features like surges visible in Hα images (*1–6*, same numbering). Some others are different, e.g, *7* and *8* and, especially, deep, long-lived dimmings. They show up as two regions *D1* and *D2* near the post-eruptive arcade, a dark arch connecting their tops, and a V-like dark feature on top of the arch. By comparing panel *h* with *a* and *e*, one can see that these deep, long-lived dimmings are due to significant darkening or disappearance of rather compact coronal structures, which were previously bright. By contrast, dimmings with shorter lifetimes, which have pronounced counterparts in Hα images, are probably due to absorption of the 195 Å emission in ejected material.

Running-difference images in Figure 5b–f show faint, shallow disturbances to embrace the whole NW quadrant of the solar disk during 00:24–01:26. A shallow depression (SD) moving toward the North Pole is also faintly visible in fixed-base difference images (Figure 4d,g,h).

The TRACE field of view is insufficient to cover D1 and D2 dimmings. Its 173 Å images in Figure 6 show that the arch-like dimming is due to eruption of loop *L1*. Dimming D2 is due to changes of the loop system near the western leg of the filament. The TRACE 173 Å and EIT 195 Å bands do not coincide that explains some differences in their images.

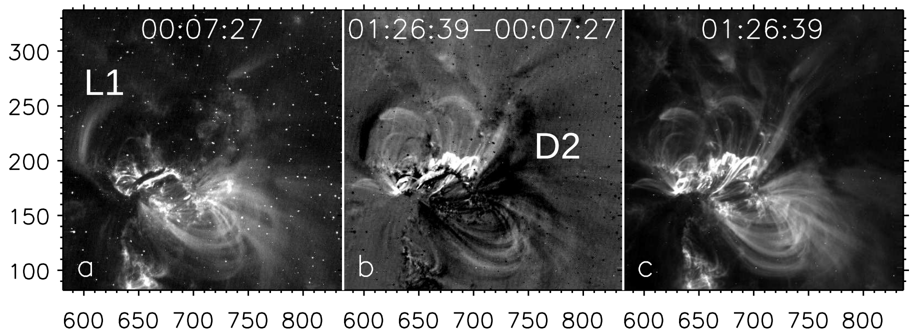

Figure 6. TRACE 173 Å images before (a), after (c) the eruption and their difference (b).

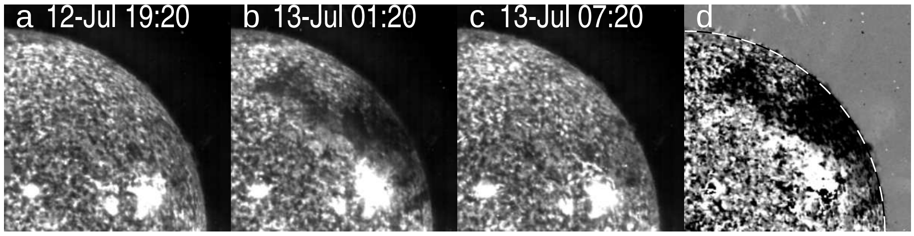

Figure 7. The northwest quadrant of EIT 304 Å images produced before (*a*), during (*b*), and after the event (*c*); (*d*) difference image, *frame (b) minus frame (a)*. Solar rotation compensated for all images to 00:40. Dashed circle in panel *d* denotes the solar limb.

2.4. Large-Scale Darkening in the SOHO/EIT 304 Å Channel

SOHO/EIT observed a large-scale darkening in the 304 Å band in a single frame at 01:20 (Figure 7). Panels *a*–*c* show three sequential full-disk solar images produced in the SOHO/EIT 304 Å channel. They are separated by 6 hours, which rules out a possibility to study development and motion of the dark feature. It is certainly absent in the first (*a*) and last (*c*) frames, whereas it is well pronounced in frame *b*. Figure 7d shows a difference image between the middle (*b*) and first (*a*) frames with a brightness limited from both sides. The area bounded by −25% depression amounts to 6.7% of the whole area of the solar disk, while the deepest depression reaches −60%. Besides the on-disk darkening, faint off-limb ejecta are also seen against the sky in the last panel. The configuration of the large-scale darkening is completely different from those observed in the 195 Å band.

2.5. Ejecta Observed with NoRH at 17 GHz

The flare produced a strong microwave burst at 17 GHz, with its main phase lasting until 00:19 and a maximum brightness temperature up to

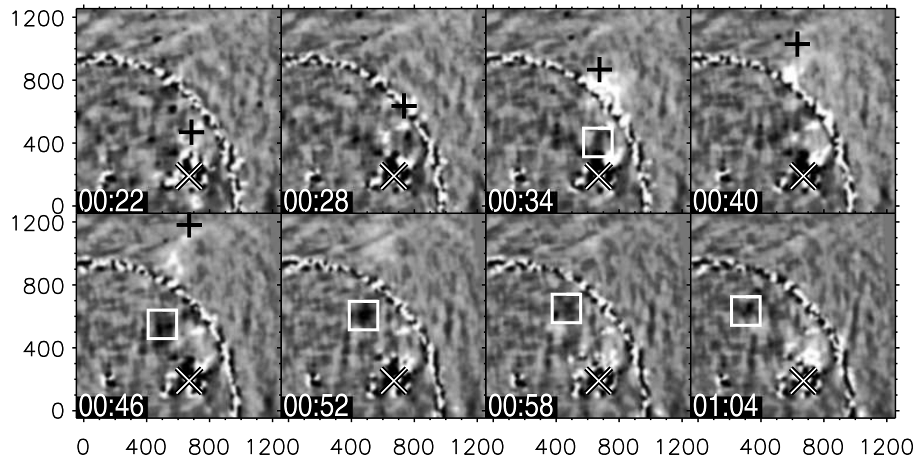

Figure 8. NoRH 17 GHz difference images (nonlinearly displayed). Black crosses mark the measured leading edge of the bright feature. White squares mark the measured center of the dark feature. Slanted cross marks the eruption center.

$T_\mathrm{B} = 1.2 \cdot 10^8$ K (T_B = 10 000 K for the quiet Sun at 17 GHz). To reveal faint moving features, we produced enhanced-sensitivity NoRH images at 17 GHz with a long integration time of 1 min. Figure 8 shows a set of such images. The moving features are still poorly visible, especially when the flare has not yet ceased. Nevertheless, using extra averaging over three frames and subtraction of an image averaged during 01:41–01:50, it is possible to detect two moving features in 17 GHz images.

One of them is dark and moves toward the North Pole (white squares mark its center in Figure 8). Its lowest brightness temperatures reach 6 000–8 000 K against the background of the quiet Sun (10 000 K), which obviously points at its large optical thickness and, consequently, the kinetic temperature of $\lesssim$ 6000 K. The other feature is bright and moves up in the sky plane. Black crosses in the figure mark its roughly measured leading edge. It becomes pronounced, when it leaves the solar disk, but this is probably due to its partial overlap with the dark feature, when they are not far from the eruption region. Thus, this feature is probably optically thin. Its measured brightness temperatures are 400–5 000 K; hence, its kinetic temperature is probably $\gg$5 000 K. Its estimated velocity is $\sim$ 500 km s^{-1}, close to the speed of the bright feature *F1* visible in TRACE 173 Å images, and the directions of their motion are also close.

2.6. CME in SOHO/LASCO/C2 Images

SOHO/LASCO/C2 & C3 observed a CME with a central position angle of 294° in many frames from 00:54 onwards. The CME was classified in the

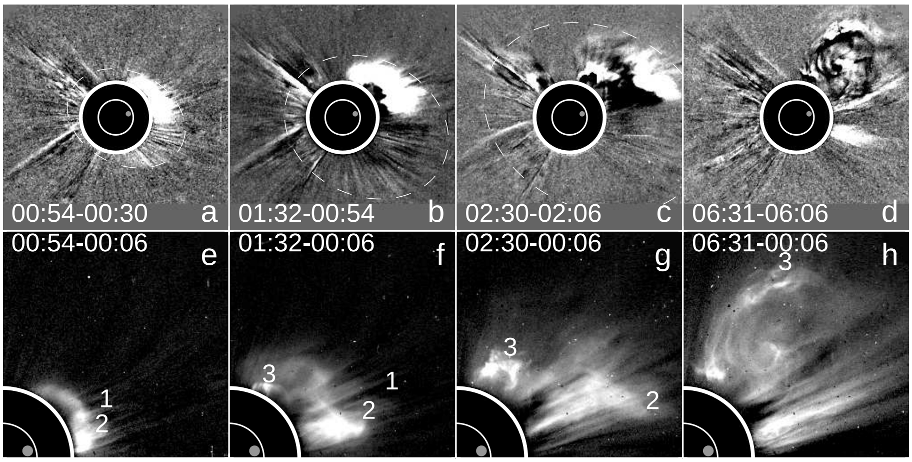

Figure 9. LASCO/C2 images of the related CME: running differences (*a–d*) and fixed-base differences (*e–h*, NW quadrant). All images are nonlinearly displayed. Thin circle: the solar limb, thick circle: occulting disk, small gray disk: the position of the eruption region, white dashed ovals outline the expanding CME. Labels denote discussed features.

Preliminary 2004 SOHO LASCO Coronal Mass Ejection List[3] as a 'partial halo'. Figure 9 shows four of LASCO/C2 images. The bright part of the CME has an angular span $< 90°$. The spatial structure of the CME does not match a classical three-component one. Its components do not resemble a self-similar structure with each one being inside another one. No cavity is detectable. The foremost part of the CME does not look like a well-defined frontal structure. It factually consists of ragged, diffuse, faint material, inside which an interconnected structure is visible (frame *f*).

Label *1* marks the fastest spike-like feature used for measurements in the SOHO LASCO CME Catalog[4]. Its linear-fit speed is 409 $\mathrm{km\,s^{-1}}$. Labels *2* and *3* mark the brightest components of the CME. Component *3* rotates that shows up in its helical structure. Ejected material is detectable around almost the whole occultor, but it is very faint in position angles $0 - 270°$, even with respect to the foremost NW part (the fainter, faster SW part is listed in the SOHO LASCO CME Catalog as another CME). The white dashed ovals in Figure 9 approximately outline the whole expanding CME.

The position angle, at which feature *3* appears from behind the occultor, corresponds to the direction, in which bright features in NoRH 17 GHz and TRACE 173 Å (*F1*) images move. Its shape somewhat resembles the shape of the 17 GHz feature. The position angle of feature *2* approximately

[3] ftp://lasco6.nascom.nasa.gov/pub/lasco/status/LASCO_CME_List_2004
[4] http://cdaw.gsfc.nasa.gov/CME_list/

corresponds to the directions of feature *F2* in TRACE 173 Å images and the bright sector visible in the EIT 195 Å image at 00:24.

2.7. Total Flux Radio Data

Total flux records of the radio emission made with Nobeyama Radio Polarimeters (NoRP) and in Learmonth and Ussuriysk Observatories initially show a strong burst starting from about 00:12:20 with its peak values up to 1200 sfu at 17 GHz. Then, starting from 00:30–00:40, a post-burst decrease is observed at frequencies ≤ 5 GHz by 01:15–01:50 (Figure 10). The duration of the 'negative burst' is minimal at 5 GHz and increases toward lower frequencies as well as the depression depth, from 5% at 5 GHz to 12% at 1 GHz. The deepest depression occurs at 00:55. The large-scale darkening is registered in the EIT 304 Å channel at the final stage of the 'negative burst'.

Drifting bursts at lower frequencies have been reported by several observatories, with strong type II bursts being observed from 00:16 till 00:43 at 300 to 20 MHz. The estimated shock speeds decrease from 1000 $\mathrm{km\,s^{-1}}$ (00:17–00:20) via 850 $\mathrm{km\,s^{-1}}$ (00:16–00:40) to 550 $\mathrm{km\,s^{-1}}$ (00:27–00:41).

2.8. Overall Picture of Near-Surface Activities

Figure 11 presents an overall picture of large-scale disturbances observed on the solar disk and in its closest vicinity during and after the 13 July 2004 eruptive event. The figure summarizes observations in the Hα line, in 195 Å, 304 Å (EIT), and 173 Å (TRACE) bands as well as at 17 GHz (NoRH).

The observable manifestations of the event start at 00:02:30 with stretch of the filament or two 'merged' filaments (acceleration of $\simeq 16\,\mathrm{m\,s^{-2}}$). During its steady rise, energy release starts beneath (by 00:13:40) that shows up as flaring in TRACE images and microwaves. At about 00:15, the filament erupts. The eruption produces Moreton and 'EIT' waves, whose velocities exceed those of all other observed disturbances. Dark fragments of the filament fly mostly north of the active region, form surges, and even reach vicinities of the North Pole. Bright material also moves north, with one its portion going straight up in the sky plane, while another one going west-northwest. The former portion is well traceable in TRACE 173 Å and NoRH 17 GHz images from the eruption site up to the edge of the field of view. The latter one is only weakly pronounced in TRACE 173 Å images.

3. Absorption

As multi-spectral data show (Figure 11), fragments of the eruptive filament dispersed over a large area could be responsible for absorption phenomena observed in radio range ('negative burst'), Hα (surges), and EUV at 195 Å

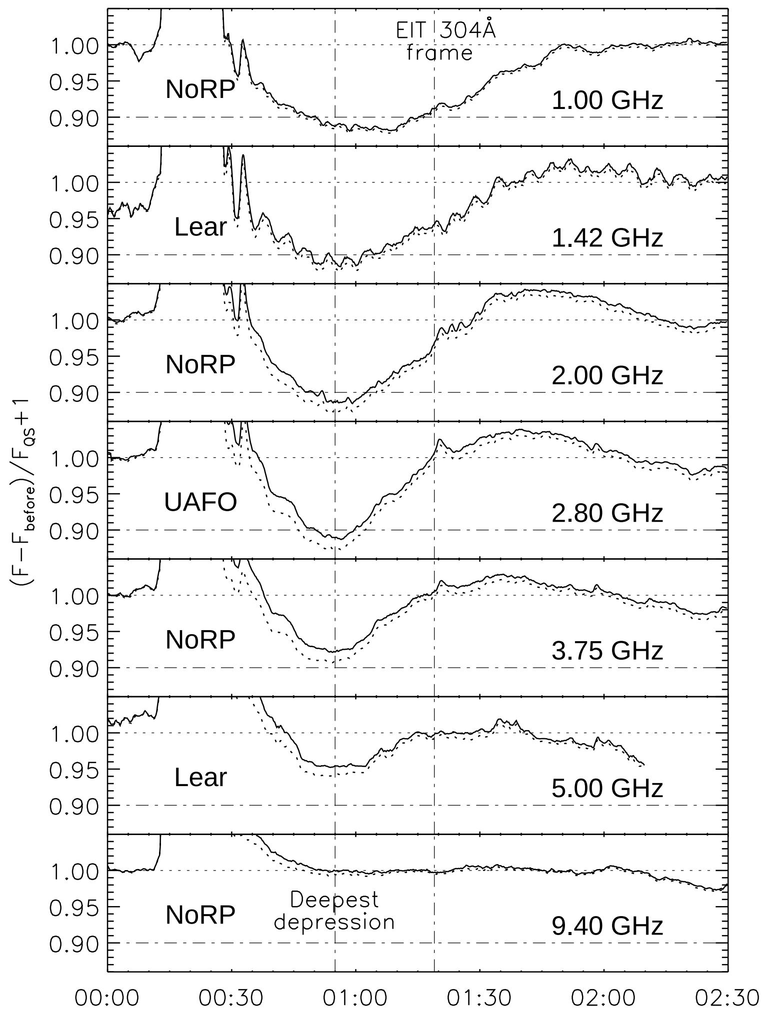

Figure 10. Total flux time profiles in a range of 1–9.4 GHz recorded in Nobeyama, Learmonth, and Ussuriysk observatories. Dotted lines show subtracted free-free emission of the arcade computed from soft X-ray GOES data.

and 304 Å. In this section, we estimate parameters of absorbing material and find out if it is possible to reconcile all mentioned manifestations. We then compare the estimated masses of the absorber and the CME.

3.1. Simulation of Radio Absorption

It seems to be hardly possible to construct a realistic model of the absorption phenomena in the radio domain under large uncertainties, which are present. Nevertheless, we try to simulate the 'negative burst' using a simple four-layer

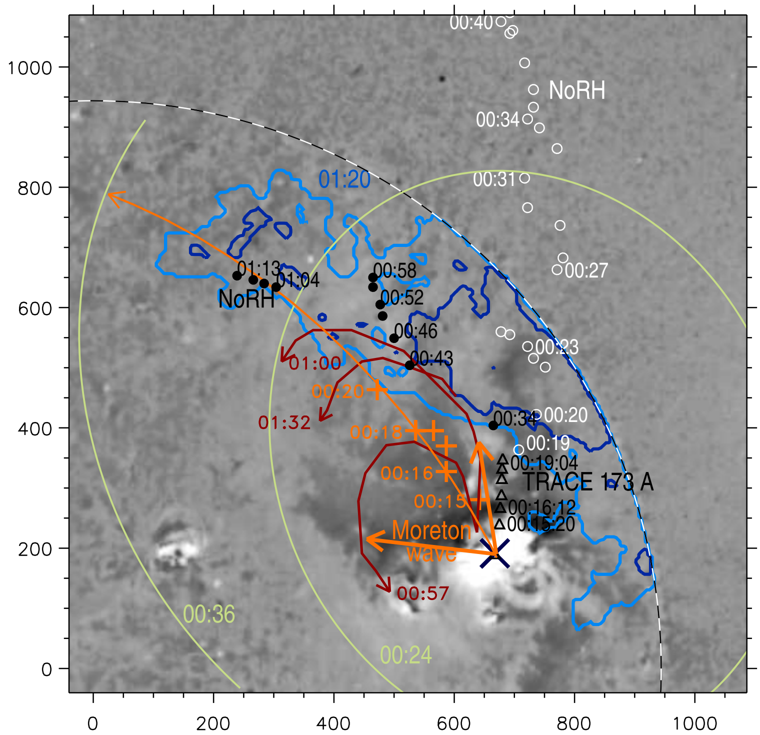

Figure 11. An overall map of large-scale disturbances observed during the event on the solar disk and in its vicinity. Gray scale background: the EIT 195 Å difference image (00:24–00:00). Blue contours: darkening in the EIT 304 Å image (13 Jul, 01:20 − 12 Jul, 19:20); bright −20%, dark −60%. Green-yellow oval and arc: wave fronts in the EIT 195 Å difference images (00:24 and 00:36). Black slanted cross: eruption center. Red crosses: measured position of the Moreton wave fronts. Red arc with the arrow: approximate propagation direction of the wave along the solar surface; red arrows roughly show its angular span. Three brown arrows: trajectories of moving fragments, which were revealed from MLSO Hα images. Triangles: the leading edge of the expanding bright feature in the TRACE 173 Å images. Circles: measured positions of the moving bright (white) and dark (black) features in NoRH 17 GHz images. Black-white dashed circle: the solar limb.

model with a uniform absorbing slab. The model shown in Figure 12 contains 1) the chromoshpere, 2) the 'spray' of area A_S 'inserted' into the corona, 3) the coronal layer of depth z between the chromosphere and the spray, and 4) the coronal layer between the spray and the observer. The optical thickness $\tau_i = k_\nu L_i$ of an $i^{\rm th}$ layer at a frequency ν, a depth of L_i, and a kinetic temperature of T_i is determined by an expression (CGS units)

$$\tau_i \approx 0.2 n_e^2 \nu^{-2} T_i^{-3/2} L_i. \qquad (1)$$

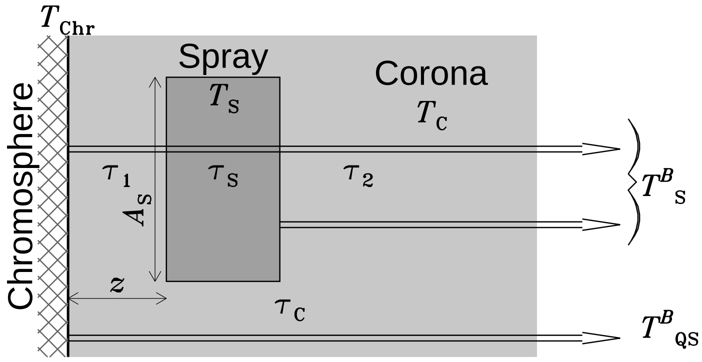

Figure 12. A simple model to estimate the frequency dependence of radio absorption.

The ratio of the observed flux to the quiet Sun's total flux is

$$F/F_{\mathrm{QS}} = [T^B_{\mathrm{QS}}(A - A_{\mathrm{S}}) + T^B_{\mathrm{S}} A_{\mathrm{S}}]/(T^B_{\mathrm{QS}} A) \tag{2}$$

The superscripts 'B' denote here the brightness temperatures to distinguish them from the kinetic temperatures. Since the brightness temperature after each layer is a sum of its own emission and an absorbed emission of preceding layers, the observed brightness temperature of the spray is

$$\begin{aligned} T^B_{\mathrm{S}} = T_{\mathrm{Chr}} e^{-(\tau_1+\tau_2+\tau_{\mathrm{S}})} + T_{\mathrm{C}}(1 - e^{-\tau_1}) e^{-(\tau_2+\tau_{\mathrm{S}})} \\ + T_{\mathrm{S}}(1 - e^{-\tau_{\mathrm{S}}}) e^{-\tau_2} + T_{\mathrm{C}}(1 - e^{-\tau_2}) \end{aligned} \tag{3}$$

where τ_i is determined by expression (1), and $\tau_1 = \tau_{\mathrm{C}} - \tau_2$, with τ_{C} being the total optical thickness of the corona at a given frequency, $\tau_2 = \tau_{\mathrm{C}} e^{-2z/H}$, $H = 2kT_C/(m_i g) \approx 8.4 \cdot 10^9$ cm the height of the uniform atmosphere, k Boltzmann constant, z the height of the absorbing layer above the chromosphere, m_i the average mass of ions, and g the gravity acceleration.

Using this simple model, we fitted the absorption depth measured from total flux records at several frequencies (Figure 10) for two instances, the maximum radio absorption (00:55) and EIT observation at 304 Å (01:19). The results are shown in Figure 13 along with parameters, which supplied the best fit. Our model is coarse; nevertheless, variations of parameters of ±20% cause detectable discrepancies with observations.

Assuming plausible ranges of the geometrical depth L of absorbing material, the fitted quantities obtained in our simulations allow estimating its mass m from expression (1), $m \sim (1.8 - 5.7) \cdot 10^{15}$ g with $L = 20 - 200$ Mm at 00:55 and $m \sim (1.2 - 4) \cdot 10^{14}$ g with $L = 5 - 50$ Mm at 01:19.

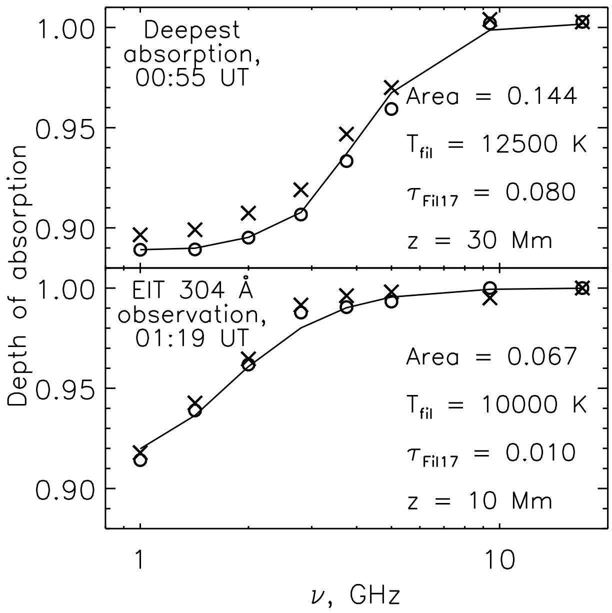

Figure 13. Radio absorption measured directly (crosses) and with subtracted contribution from the arcade (circles) along with results of modeling (lines) for two instants.

3.2. Absorption in Hα and EUV

Hα opacity is due to neutral hydrogen, which absorbs the continuum radiation from underlying atmosphere. Mein *et al.* (1996); Heinzel, Mein, and Mein (1999); Molowny-Horas *et al.* (1999), and Tziotziou *et al.* (2001) carried out detailed calculations of physical parameters in still or slowly moving cool clouds like filaments on the basis of a non-LTE radiative transfer approach. Heinzel *et al.* (2001, 2003a) studied relations between opacities in Hα and Lyman continuum at 912 Å and proposed an approximate expression to estimate the hydrogen density from the optical thickness of the Hα line center. Absorption of moving prominences decreases due to the so-called Doppler-brightening effect with a line-of-sight velocity exceeding typically 50 $\mathrm{km\,s^{-1}}$. For BBSO Hα filtergrams produced with the 0.5 Å Lyot filter, this effect appears at a lower velocity of $\sim$ 20 $\mathrm{km\,s^{-1}}$, when the Doppler shift of the Hα absorption line exceeds the bandwidth of the instrument.

A spectroscopic model for absorption of EUV emission in filaments and prominences was developed by Heinzel *et al.* (2003a,b), Anzer and Heinzel (2005), and Schwartz *et al.* (2006). They showed that the EUV opacity is due to photoionization of hydrogen (below the edge of the Lyman continuum 912 Å), neutral helium ($<$ 504 Å), and ionized helium ($<$ 228 Å). Absorption of continuum does not depend on radial or turbulent velocity. For 195 Å,

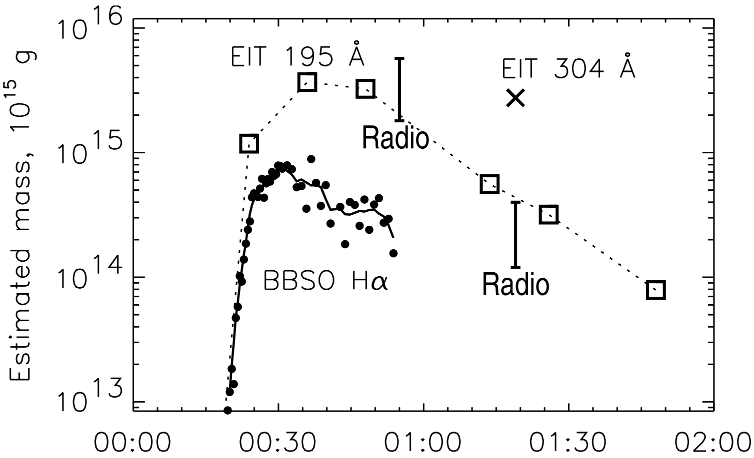

Figure 14. The mass of the ejecta estimated from opacities in Hα (circles), 195 Å (squares), 304 Å (cross), and radio range (bars).

we take an average absorption cross-section of a 'cloud' consisting of 92% of H and 8% of He, $\sigma_{195} \approx 7 \cdot 10^{-20}$ cm^2, which varies within 30–40% in a temperature range of $0 < T < 80\,000$ K. Along with absorption, darkening in coronal lines could be due to a volume blocking effect (VBE), i.e., the absence of a coronal radiation from the volume of the cloud. This effect depends on the height and depth of the cloud in comparison with a height scale at a given wavelength. For 195 Å, a typical radial height scale is ~ 70 Mm, and for our position angle, 42°, the line-of-sight height is $H_{\|} \sim 100$ Mm.

Using BBSO Hα images, we computed the hydrogen density from the optical thickness of the Hα line center. We assumed a line-of sight velocity $V_{\|} < 20$ km s^{-1}, turbulent velocity $V_{\rm turb} = 5$ km s^{-1}, temperature 8 000 K, and depth of each absorbing fragment to be equal to its width. Figure 14 presents total masses estimated from absorption of all considered emissions. The mass estimated from Hα increases from 00:14 by 00:30 and then diminishes likely because velocities of fragments become $V_{\|} > 20$ km s^{-1}.

To estimate the opacity at 195 Å, we analyzed the EIT difference images in the interval of 00:12–02:00 with a reference image of July 12, 23:59:57. Regions of probable absorptions were found as depressions below 1σ level, where σ was computed as a r.m.s. over negative values of a difference image within the NW quadrant (i.e., only over regions of decreased brightness). The regions revealed by means of this criterion incorporated long-lived dimmings (e.g., *D1* and *D2*), which are unlikely to be due to absorption. They are identifiable in the difference image at 02:00; we excluded them from computations. The mass estimated from 195 Å images reaches its maximum of $3.7 \cdot 10^{15}$ g at 00:35, and then diminishes, when the main part of the ejecta leaves the field of view of EIT. The estimations miss some fragments of the ejecta that crossed the long-lived dimmings and could contain 20–30% of the total mass. In addition, a noticeable part of the ejected mass could be contained in hot ionized plasmas of the transition layer between cold absorbing material and surrounding corona (analogous to the EUV filament channel) seen in TRACE 173 Å as a bright contour. We did not consider the VBE, because the depth of individual absorbing fragments was $\ll H_{\parallel}$.

In 304 Å, a large depression area appears at 01:19 (see Figure 7), showing some part of the ejected material to return back onto the Sun. The same selection criteria of absorption regions as for 195 Å were applied. A mean brightness ratio to the pre-event image in all selected region is about 0.54, while in a significant part of the depression region it is noticeably below 0.5.

Absorption of the 304 Å emission in the cloud can be due to photoionization of H and HeI by continuum or due to resonant scattering of the HeII line in He ions. The latter mechanism cannot provide the absorption ratio < 0.5: the cloud emits resonant photons in 4π angle, while incident photons come from below and lateral directions, i.e., 2π. Moreover, the resonant scattering is very sensitive to the line-of-sight velocity: the Doppler shift exceeds a typical width of the HeII 304 Å line if $V_{\parallel} > 50$ km s^{-1}. Absorption of the continuum is much more probable (cross section $\sigma_{304} \approx 5.5 \cdot 10^{-19}$ cm^2). An estimate of the mass is $\sim 2.8 \cdot 10^{15}$ g shown by the cross in Figure 14.

The closest images observed in the coronal bands of 171 Å (01:00) and 195 Å (01:25) do not show absorption in the 304 Å darkening region (absorption at 195 Å occurs in other regions). At this time, the cloud was likely situated above the height of HeII 304 Å illumination, but lower than coronal loops responsible for the 171 and 195 Å emissions, as absorbing flows in TRACE 173 Å images demonstrate. Low clouds with a temperature close to the chromospheric one (10 000 K) are not detectable in radio range also.

The CME mass estimated using LASCO software reaches $1.3 \cdot 10^{15}$ g at 04:06. Due to the off-plane direction of the CME, it should be corrected by a factor of ~ 1.4 (Vourlidas *et al.*, 2000); thus, its real mass is $1.8 \cdot 10^{15}$ g. Note that a lesser mass of $1.8 \cdot 10^{15}$ g given in the SOHO LASCO CME Catalog is related to the faint SW part (see Figure 9a–c).

The estimations of the mass of the ejecta obtained from absorption of different emissions agree with each other within their accuracy and obvious limitations of different methods. The masses of the CME and the part of the ejecta that returned onto the Sun are close. This means that the ejecta disintegrated into parts with comparable masses, one of which left the Sun and flew away, while another one fell back onto the solar surface. One might ask if the absorbing cloud left the Sun later and was observed as a slower feature visible in Figure 9h at approximately the position occupied by feature

3 in the previous frame. However, its estimated mass is $1.1 \cdot 10^{14}$ g, much less than the mass of the cloud. This rules out such a possibility.

4. Kinematics

In this section, we choose analytic expressions to describe kinematics of a wave expanding from the eruption site and mass fragments flying away. Their birth in a single process appears to be undoubted. However, their mutual influence in their motion is not obvious, i.e., it is not clear if a piston existed to determine the motion of the wave propagating away. The discussed observations do not reveal manifestations of a piston; the wave and fragments appear to propagate independently. A significant deceleration of mass fragments, constituting the CME, points at importance of gravity. This also shows up in the fact that some part of ejected mass falls back and produces a cool absorbing 'screen' to cover a significant part of the Sun.

4.1. Approach

Considering kinematics of observed moving features, we employ a self-similar approximation to describe the expansion of plasma pieces flying away, 'fragments of explosion'. Low (1982, 1984a,b) first applied it to a CME expansion. Uralov, Grechnev, and Hudson (2005) derived expressions, which were convenient to compare with observations. These expressions apply both under the absence or presence of a CME-driven coronal shock. In the latter case, observed CME fragments are assumed to be confined within a volume bound by a contact surface, which is also a surface of a moving piston. A used solution belongs to a class of self-similar motions, in which Lagrangian velocities of plasma pieces v are proportional to their distances r from the center of expansion, $v \propto r$ (see also Sedov, 1981, p. 318).

To describe wave-like phenomena, we employ concepts of self-similar theory of a point-like explosion (e.g., Sedov, 1981; Zel'dovich and Raizer, 1966). During such an explosion, energy release occurs, but mass does not release. Such an explosion produces a strong shock wave in an environment media.

A crude example to combine both these approaches is an air explosion of a bomb consisting from a charge and a shell. The outcome is a shock wave and fragments of the shell flying away. They expand synchronously during the explosion and move independently afterwards.

4.2. 'Fragments of Explosion'

As shown in Section 2.8, some counterparts of CME features visible in LASCO images are detectable on the Sun or nearby. Figure 15 shows distance-time points measured from TRACE, NoRH, and LASCO data. The best

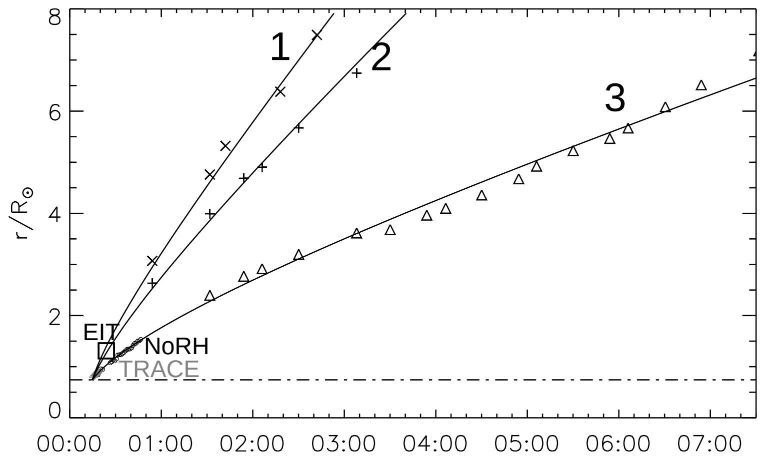

Figure 15. Distance-time plots (in solar radii) of fragments observed with TRACE at 173 Å (bright crosses), NoRH at 17 GHz (circles), and LASCO/C2 (black; slanted crosses for feature 1, straight crosses for feature 2, and triangles for feature 3). The square denotes the observation point of the bright aureole in the EIT 195 Å image at 00:24. Dash-doted line denotes the position of the eruption center.

coverage has feature 3 and its counterparts. Since only deceleration is observed for all detectable features, no polynomial fit of the measured data points applies. A quasi-periodical component in all plots is due to rotation of the ejecta that complicates measurements and decreases their accuracy.

Using expression A8 from the paper of Uralov, Grechnev, and Hudson (2005), one obtains: $v^2 = v_0^2 + 2A/r_0\,(1 - r_0/r)$ with $r \to \infty, v \to v_\infty$ and $v_0 = v(r = r_0)$ gives $2A/r_0 = v_\infty^2 - v_0^2$, and

$$v^2 = v_0^2 + \left(v_\infty^2 - v_0^2\right)(1 - r_0/r)\,. \tag{4}$$

We integrated this expression numerically. To compare results with observational data, a few parameters are necessary; the initial and asymptotical velocities, v_0 and v_∞; the initial size of the ejecta, r_0; and origins of measurements both in space and time. The origins are known with satisfactory uncertainties (see Section 4.4; start time 00:14:50). The v_∞ can be approximately taken from Figure 15 (it is 409 $\mathrm{km\,s^{-1}}$ for feature 1 according to the SOHO LASCO CME Catalog). The v_0 for feature 3 can be found from TRACE and NoRH data points. Obviously, $v_0^{(1)} > v_0^{(2)} > v_0^{(3)}$. The r_0 parameters could be only found in attempts to obtain a good fit. The curves in Figure 15 were obtained with the following parameters:

feature 1: $r_0 = 270$ Mm, $v_0 = 1100\ \mathrm{km\,s^{-1}}$, $v_\infty = 409\ \mathrm{km\,s^{-1}}$;

feature 2: $r_0 = 220$ Mm, $v_0 = 850\ \mathrm{km\,s^{-1}}$, $v_\infty = 310\ \mathrm{km\,s^{-1}}$;

feature 3: $r_0 = 110$ Mm, $v_0 = 490$ km s^{-1}, $v_\infty = 100$ km s^{-1}.

These parameters provided a satisfactory fit for each of the three features visible in LASCO images, with the accuracy being worse for features 1 and 2, whose counterparts are poorly identified at/near the Sun.

4.3. Wave. Uchida's Model: Weak Fast Mode

The almost perfect oval shape of the brightening in the EIT 195 Å image at 00:24 and its expansion visible in the next image at 00:36 are suggestive of its wave-like origin and its association with the Moreton wave. The following facts also support this: (i) its configuration is different from the main observed CME components, in particular, (ii) its eastern part is roughly as bright as the western part, if not exceeds it, whereas the eastern CME part in LASCO/C2 images is much fainter than its western part, and (iii) the apparent velocity of the oval, $\simeq 700$ km s^{-1}, is comparable with the Moreton wave's one. This possibility was previously discussed by, e.g., Hudson and Warmuth (2004) and Warmuth *et al.* (2001, 2004a, 2004b).

According to the original Uchida's (1968) idea, a Moreton wave is excited by a coronal wave, being its lower outskirt. As for a particular model, Uchida (1968) considered a weak short fast-mode MHD wave to propagate in a radially-symmetric corona, with the Alfvén speed increasing with height (which was uncertain at that time). This resulted in refraction of rays into regions of lower Alfvén velocity, i.e., toward the solar surface, and a corresponding turn of the wave front. The model also predicted acceleration of Moreton waves, although Warmuth *et al.* (2001, 2004a) found their systematic deceleration (Yamaguchi *et al.* (2003) reported acceleration of a Moreton wave in its propagation into a coronal hole). Their observed velocities are sometimes too high for weak fast-mode MHD disturbances; in addition, the large observed thicknesses of the wave front that sometimes linearly increase with distances (Warmuth *et al.*, 2001, 2004b, 2005) are incompatible with this mechanism, but suggest a self-similar expansion after an initial explosion. These inconsistencies with observations do not appear to rule out the weak fast-mode MHD disturbance completely, but nevertheless encourage to search for another possibility to match observational facts better. Warmuth *et al.* (2001, 2004a, 2004b) and Hudson and Warmuth (2004) proposed blast waves to be responsible for Moreton waves and, probably, some 'EIT waves'.

4.4. Wave. Strong Shock

We use estimative expressions from a theory of a strong point-like explosion in a variable-density medium. A rigorous analysis of this gas dynamic task can be found, e.g., in a book of Sedov (1981). Self-similarity of a solution is ensured by large pressure excess inside the volume confined by the shock front over non-disturbed medium. If a magnetic field in non-disturbed unbounded plasma is strong (whereas the fast shock propagates over quiet Sun in our event), then the wave profile and the shape of the shock front changes. This change is small for a strong shock, because the increase of the magnetic pressure in the shock is determined by extreme plasma compression, whereas gas pressure is not limited.

Kinematics of a single-pulse spherical blast wave is governed mainly by a pile-up mass. We consider propagation of a self-similar blast wave excited by an explosion of an energy E in media (a) with a constant density, and (b) with a radial density falloff from the explosion center, $\rho \propto r^{-\alpha}$.

- For a constant density, $\rho = \rho_0$: $\rho_0 R^3 V^2 = const\ E$ (R and V radius and velocity of the shock front), with *const* corresponding to constancy of potential to kinetic energy ratio for plasma involved into self-similar motion. Thus, $V = \frac{dR}{dt} = \left(\frac{const\ E}{\rho_0 R^3}\right)^{1/2} \propto R^{-3/2}$, and $R \propto t^{2/5}$.
- Similarly, for $\rho = br^{-\alpha}$: $V^2 \int \frac{b}{r^\alpha} r^2 dr \to V^2 R^{[3-\alpha]} = const\ E$. Consequently, $V = \frac{dR}{dt} \propto R^{-[(3-\alpha)/2]}$, and

$$R \propto t^{[2/(5-\alpha)]} = t^\delta. \tag{5}$$

A strong spherical shock wave decelerates if $\alpha < 3$ and accelerates if $\alpha > 3$. Thus, $\delta = 2/(5-\alpha)$, with $\delta = 0.4$ for a homogeneous medium ($\alpha = 0$) and $\delta = 0.67$ for a medium with $\rho \propto r^{-2}$. To compare expression (5) with measured points of the Moreton wave, we use expression (5) in a form $(R - R_0)/(R - R_1) = [(t - t_0)/(t - t_1)]^{[2/(5-\alpha)]}$. Here R_0 are the distance between the origin of measurements and explosion center and t_0 the corresponding time, and t_1, R_1 are related to one of measured points.

The results are shown in Figure 16, where the last point measured for the Moreton wave is used as a reference one (t_1, R_1). The long-dashed curve corresponding to $\alpha = 0$ shows much stronger deceleration than factually observed. A surprisingly good fit is achieved with $\alpha = 2$ ($\delta = 0.67$) and the start time of 00:14:50 for both the Moreton wave and the 'EIT wave' oval. The dotted and dashed curves plotted for the start time of 00:14:50±20 s demonstrate that the uncertainty of the t_0 is small. Similarly, the positional uncertainty of the explosion center does not exceed 20 Mm; origins of both the position and time are close to the observed eruption ones.

The kinematical closeness of the Moreton wave and 'EIT wave' confirms they common nature. Their closeness to the calculated distance-time plot supports their origin due to coronal blast shock. Note also that the farthest point of the 'EIT wave' at 00:36 suggests a stronger deceleration, thus implying the density falloff to be $\alpha < 2$ at longer distances.

The calculated instant speed of the strong shock for $\rho \propto r^{-2}$ shown in Figure 16 is interesting to compare with estimates of the shock speed

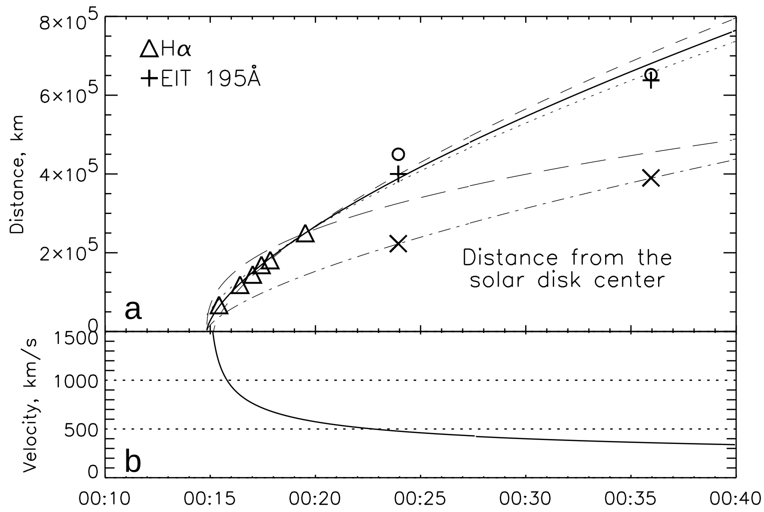

Figure 16. (a) Distance-time plots of the Moreton (triangles) and 'EIT' waves (crosses) measured in the same direction from the eruption center and (b) the instantaneous velocity computed for $\rho \propto r^{-2}$. Circles denote the foremost parts of the 'EIT wave'. Curves: fits with $\rho = const$ (long-dashed), $\rho \propto r^{-2}$ (solid at t_0 = 00:14:50, dotted at t_0 = 00:15:20, and short-dashed at t_0 = 00:14:20). Slanted crosses: the positions of the oval towards the solar disk center; dash-dotted curve shows their fit with $\rho \propto r^{-2}$.

from type II bursts. The estimated speeds decrease from 1000 km s^{-1} at 00:17–00:20 via 850 km s^{-1} (00:16–00:40) to 550 km s^{-1} at 00:27–00:41. Such estimations are based on model plasma densities, which have large uncertainties. Nevertheless, the overall agreement of variations of the calculated shock speed with the estimated ones from the type II drift rate seems to be convincing. This favors the same origin of the Moreton wave and 'EIT wave', on the one hand, and the type II radio burst, on the other hand. All these phenomena are likely associated with the same decelerating coronal blast shock, as Warmuth *et al.* (2001, 2004a, 2004b) concluded. Another interpretation is discussed by Pohjolainen, Hori, and Sakurai (2007).

Moreton wave runs parallel to the surface and presumably presents a trace of a strong coronal shock front moving to the same direction. If so, then one should assume that the falloff of the coronal density in this direction is the same as it upwards is – at least, in this event. Otherwise, e.g., with a density being constant at a given height, the wave decelerates even stronger than expression (5) with $\alpha = 0$ predicts. To crudely estimate such a case, we consider a vertically-stratified atmosphere with a density falloff upwards of $\rho \propto r^{-\alpha}$. After an explosion in such atmosphere, the shape of the wave surface is not a spherical one. The shock front propagating horizontally from the explosion center inclines down, and the inclination progresses. We assume pressure P to be uniform inside a volume confined by the shock front, $P \propto \frac{E}{R^3}$ with R being the largest, vertical size of the wave surface. Its variation is determined by expression (5). In a strong shock, $\rho_x V_x^2 \simeq P$, where $V_x = \frac{dR_x}{dt}$ is a velocity of the shock front running along a constant-density surface, $\rho_x = const$. With $\alpha = 2$, $V_x \propto t^{-1}$, and $R_x \propto \ln(t)$. The extremely strong deceleration of the wave means that after its fast onset, the wave almost stops (sometimes observed for 'EIT waves').

Besides the assumption of the same density falloffs both up and sideward from the eruption center, one more possibility exists to prevent strong deceleration of a strong coronal shock running along the solar surface, i.e., a piston moving in the same direction with a proper deceleration (cf. Low, 1984a). If a self-similar solution does exist, then a piston and a wave of a common origin diverge rather slowly. Indeed, the velocity of the strong shock front is $\frac{dR}{dt} = \frac{\gamma+1}{2} v_{\mathrm{sh}}$ with γ the polytropic index, and v_{sh} Lagrangian plasma velocity just behind the shock front. The velocity of the contact discontinuity is $\frac{dr_{\mathrm{c}}}{dt} = v_{\mathrm{c}}$ with v_{c} Lagrangian plasma velocity within the discontinuity. In self-similar motions of the considered kind, $\frac{v_{\mathrm{sh}}}{v_{\mathrm{c}}} = \frac{R}{r_{\mathrm{c}}}$. From these expressions, $\frac{dR}{R} = \frac{\gamma+1}{2} \frac{dr_{\mathrm{c}}}{r_{\mathrm{c}}}$. Thus, the ratio of positions of the shock front R and the piston r_c with respect to the explosion center is $\frac{R}{r_{\mathrm{c}}} \propto r_{\mathrm{c}}^{(\gamma-1)/2}$. If initially $R = r_c = 1$, then this ratio increases slowly, and both the piston and wave are expectable to be seen not far from each other in images, which we showed. Nevertheless, the wave appears to have run far away well before the appearance of first manifestations of the mass motion in the same direction. In favor of the blast wave rather than a piston wave evidences its oval shape, with the initial velocity vectors of the ejected mass to be apparently directed up.

We also fitted the oval envelope of the CME. A satisfactory fit was obtained with $\rho \propto r^{-2.7}$, expectable for a wave propagating outward into the corona: the upward density falloff in the corona above an active region at heights of $(0.2 - 10)R_{\odot}$ goes $\propto r^{-2}$ (r the distance from the photosphere) according to Newkirk model (Newkirk, 1961), and $\rho \propto r^{-2.9}$ from a model compiled by Gary (2001). This fit is close to the fit of feature 1 in LASCO images. Note that with $v_{\infty}^2 \ll v_0^2$ and $\alpha = 2$, expressions (4) and (5) predict the same height-time plots. Poor measurement accuracy does not allow to distinguish between the wave and fragments. Their closeness is also possible.

4.5. Comments on a Realistic Situation

Thus, there are the following possibilities for the Moreton wave.

- *Uchida's (1968) refraction model* predicts acceleration of a wave. It does not describe the observed situation. This is a linear acoustic approximation, which is very sensitive to variations of media parameters.

• *Strong shock wave.* Deceleration naturally appears, but it is too strong. To explain it, we assumed a density falloff from the explosion center to be the same both up and sideward. This appears to be reasonable while distances are moderate, but it hardly could be true of long distances (note also strengthening of deceleration hinted by Figure 16). This is a strongly non-linear case, not well sensitive to a media (mass pile-up only).

• *Shock wave of a moderate intensity*, or initially strong wave, and then a moderate wave, represents a most realistic case.

The fact that the best fit for the Moreton and 'EIT' waves corresponds to $\alpha = 2.0$ is probably accidental. Our assumptions are idealized, which certainly affects results. We assumed a strong blast wave, which in reality could have an intermediate intensity. We also assumed a radial density falloff from the explosion center, which in reality should be anisotropic and probably variable. The shape of the wave front is also important; the rate of pile-up mass grows with distance in a spherical wave faster than in a flat wave.

In a realistic situation, some range of parameters could be expected. Warmuth *et al.* (2001, 2004a, 2004b) found the average power-law indices δ for Moreton waves' distance-time plots of 0.57–0.62, which corresponds to density falloffs of $\alpha = 1.49 - 1.77$ for spherical waves. The whole range of indices they measured was mainly from 0.41 to 0.91 ($\alpha = 0.12 - 2.8$), with two exceptional cases, 0.29 and 0.34. Both those events were located on the limb, which made correct identification of wave fronts difficult; however, such strong damping and deceleration were, in principle, possible if an explosion occurred in a medium with a uniform horizontal density distribution.

The power-law distance-time relations found by Warmuth *et al.* (2001, 2004a, 2004b) and in our event are expectable for blast waves propagating in the corona, in accordance with a conclusion of Balasubramaniam, Pevtsov, and Neidig (2007) and the original idea of Uchida (1968) in its general form. Excitation of a filament by a Moreton wave from its upper edge in the 6 December 2006 event also could be due to an incident coronal front inclined down (Gilbert *et al.*, 2007). The nature of Moreton waves due to self-similar coronal shocks is supported by linear growths of the wave front thicknesses with distances estimated by Warmuth *et al.* (2001, 2004a, 2004b, 2005) for some events. It is also supported by correspondence with LASCO data.

5. Discussion and Conclusion

5.1. The Overall Scenario of the Event

The event started with a steady rise of a filament in the active region at about 00:02:30. Then an explosive eruption occurred at about 00:14:50, probably due to mergence of two close filaments. Uralov *et al.* (2002) argued explosive development of an MHD instability in such a case, and Hansen, Tripathi, and Bellan (2004) confirmed this experimentally. The eruption was probably driven by MHD forces, because the filament(s) itself remained cool while observed. The fastest observed feature accelerated up to 400–500 $\mathrm{km\,s^{-1}}$ in about 2 minutes (acceleration $> 8\ \mathrm{km\,s^{-2}}$). Since it was bright, it had a coronal temperature (at least, its part). The acceleration and speed of the cool filament(s) were less by a factor of $\gtrsim 2$.

The initial energy of the ejecta was partially spent to disperse the filament(s) over large area and to produce a shock. The remainder energy was insufficient for all fragments to overcome gravity; features were observed both to move away and to return to the Sun. The role of gravity is also manifest in deceleration of all observed features. Since the ejecta disintegrated, the CME did not resemble a classical three-part structure with self-similar frontal structure, cavity, and core, which is difficult to identify. One part of the ejecta flew away as the CME, and another one fell back onto the Sun. Masses of both parts were close. The latter part consisted of broken filament(s) fragments dispersed like a cloud to cover almost the whole NW quadrant. The cloud absorbed background emissions that caused moving dimmings in EUV and a 'negative burst' in the radio range. This cloud later landed back on the solar surface. Other fragments produced surges visible in Hα up to ~ 100 Mm. Their speeds were, at least, twice less than the speed of the fastest feature ($\sim 500\ \mathrm{km\,s^{-1}}$). Therefore, the CME in this event was mainly hot, while the returned part was mostly cool, about 10 000 K.

The eruption produced a decelerating coronal blast shock. The presence of a wave is demonstrated by a displacement of loop *L1* at 00:15:20 and 00:16:12, when the observed ejecta was far from it (Figure 3i,j). The lower outskirt of the shock was seen as a Moreton wave decelerating from the initial speed of > 1000 to $\simeq 600\ \mathrm{km\,s^{-1}}$, while it was observed. At longer distances, the shock was observed as an 'EIT wave' with a speed of $< 500\ \mathrm{km\,s^{-1}}$.

The initial magnetic structure was closed and confined inside the filament(s). After the eruption, dispersed fragments flew along lengthy field lines toward the North Pole and landed on a huge area. Some magnetic structure was carried away by the CME, as its rotation demonstrates. It is difficult to reconcile these facts without reconnection. Its role in the event is not clear. Probably, just the destruction of the magnetic configuration could cause dispersing the ejecta rather than its ejection as a whole. Anyway, reconnection does not seem to be directly related with the observed 'EIT wave' and dimmings.

5.2. Comments on Nature of Large-Scale Disturbances

The bright oval of the 'EIT wave' in this event was likely due to the coronal blast shock. This conclusion is based on the agreement of its kinematic, which is common with the observed Moreton wave, with a theoretically expected propagation of a shock. Correspondence to parameters of the type II radio burst confirms this conclusion. The spheroidal shape of the wave front reinforces it. A comparison of quantitative parameters inferred from the analysis of this event with results of other authors obtained in their analyses of several other 'Moreton & EIT wave events' shows them to be mainly consistent with their origin due to coronal blast shocks. Such phenomena are probably due to moderate-intensity shocks, or initially strong waves subsequently damping to moderate waves. Shocks generally compress (therefore brighten) and heat material. Manifestations of heating were presumably found in observations of some 'EIT waves' (Grechnev *et al.*, 2005; see also Warmuth, Mann, and Aurass, 2005).

Trailing brightenings visible in Figure 5b north, north-northeast, east-southeast of the eruption center, and a sector above the NW limb moved slower, had different shapes, and their nature was probably different. On-disk brightenings could be similar to the off-limb feature. However, they could be due to some processes in very low coronal layers, i.e., different from the off-limb feature. Our analysis does not address this issue.

Two kinds of dimming were observed. *Shallow dimmings moving* after the oval 'EIT wave' front were due to absorption of the Sun's background emission in the moving 'cloud' of filament fragments, as quantitatively confirmed. On the other hand, as Figures 4,6 show, *deep, long-lived dimmings* (e.g., *D1*, *D2*) were due to significant changes of coronal loops, which were previously bright. Figure 4 shows that dimming *D2* was too large to be due to displacement of loops. A plasma density decrease is the most probable (if not the only) reason. Plasma density can decrease in two cases. (a) Previously closed loops open or stretch into interplanetary space that results in plasma outflows. (b) Loops slightly stretch, but do not significantly change. As can be seen, with the same number of particles in a loop, a change of its volume from V_0 to V_1 results in a corresponding change of emission measure, $EM_1/EM_0 = V_0/V_1$. Thus, stretch of a loop decreases its brightness (while compression causes brightening). In summary, deep, long-lived dimmings are likely due to *density decrease* in coronal structures and obviously cannot travel. These conclusions agree with those of Chertok and Grechnev (2005a).

5.3. Estimations of Mass from Absorption

We estimated the mass of the ejected 'cloud' from absorption in the radio range, in the $H\alpha$ line, and in EUV lines of 195 Å and 304 Å. All methods converge to a close result, $\sim 3 \cdot 10^{15}$ g, a mass of an ordinary filament (a close mass had the CME, rather massive one). This implies that such a spectacular event hardly was an exceptional one. Their consistency demonstrates such estimates to offer a promising way to evaluate masses of on-disk ejecta.

Each of these methods has advantages and limitations. Hα images distinctly show absorbing features, but estimations are uncertain of their depth and constrained to low temperatures and velocities. Estimations from 195 Å emission are not velocity dependent, but they do not say much about the temperature of the absorber and fail at low heights. Estimations from 304 Å emission are sensitive up to the transition region, but crucially depend on temperature and absorption mechanism (velocity dependence is important for the resonant scattering). Estimations from multi-frequency radio data are uncertain of the depth and fail at low heights, but they allow to estimate the temperature of material in a wide range and do not depend on velocity.

5.4. Summary and Concluding Remarks

From multi-spectral data, an overall picture of the 13 July 2004 eruptive event was reconstructed and confirmed by quantitative estimations. An explosive filament eruption occurred in an active region. The ejecta disintegrated into two parts of comparable masses, one of which flew away as a decelerating CME, and another part dispersed over almost the whole NW quadrant of the visible solar disk. The latter part absorbed background solar emission that was observed as shallow moving dimmings at 195 Å, a 'negative' radio burst, and a huge dimming at 304 Å. By contrast, deep, long-lived, immovable dimmings also observed at 195 Å in this event were likely due to density decrease in coronal structures.

Properties of both the Moreton wave and the oval faint front observed at 195 Å in this event are consistent with their origin due to a coronal blast shock produced by the eruption. Our results show what could be reasons for 'EIT waves' and dimmings in a particular event, not pretending to apply to all events. Such phenomena in some events could be due to similar reasons, and in some others not.

The appearance of the coronal blast shock, the Moreton wave, and a huge cloud of dispersed material of cool filaments were interconnected in our event. It was remarkable, but probably not an exceptional one. If indeed Moreton waves are generally due to blast shocks, then related CMEs are not expected to show a pronounced acceleration. Note that a polynomial fit in such cases is inappropriate to analyze kinematics of related CMEs.

Our results also demonstrate that useful information about eruptive phenomena could be obtained by means of the following methods. Radio observations in a range of 1–10 GHz, where the corona is optically thin, while its opacity varies by an order of magnitude, are capable of supplying parameters of ejecta. Especially valuable would be multi-frequency imaging observations. Important would be observations at 304 Å with an imaging rate of < 10 min. Masses of on-disk ejecta can be estimated from absorption.

Acknowledgements

We thank V. Yurchyshyn for supplying us with BBSO Hα data and I.L. Beigman, M.A. Livshits, S.A. Bogachev, S.M. White, F. Auchère, G.V. Rudenko, H.R. Gilbert, S. Pohjolainen, and B. Kliem for useful discussions.

We used the CME catalog generated and maintained at the CDAW Data Center by NASA and The Catholic University of America in cooperation with the Naval Research Laboratory. SOHO is a project of international cooperation between ESA and NASA. We also used data of the Big Bear Solar Observatory/New Jersey Institute of Technology, the Mauna Loa Solar Observatory/High Altitude Observatory, the Nobeyama Solar Facilities, the USAF RSTN Radio Solar Telescope Network, and the GOES satellites.

The present study is supported by the Russian Foundation of Basic Research (grants 05-02-17415, 06-02-16106, 06-02-16239, 06-02-16295, and 07-02-00101), the Federal Ministry of Education and Science (grant 8499.2006.2), and the programs of the Russian Academy of Sciences 'Solar Activity and Physical Processes in the Sun-Earth System' and 'Plasma Heliophysics'.

References

Attrill, G. D. R., Harra, L. K., van Driel-Gesztelyi, L., and Démoulin, P.: 2007, *Astrophys. J.* **656**, L101.

Balasubramaniam, K. S., Pevtsov, A. A., and Neidig, D. F.: 2007, *Astrophys. J.* **658**, 1372.

Ballai, I., Erdélyi, R., and Pintér, B.: 2005, *Astrophys. J.* **633**, L145.

Brueckner, G. E, Howard, R. A., Koomen, M. J. *et al.*: 1995, *Solar Phys.* **162**, 357.

Chen, P. F., Wu, S. T., Shibata, K., and Fang, C: 2002, *Astrophys. J.* **572**, L99.

Chen, P. F., Fang, C., and Shibata, K.: 2005, *Astrophys. J.* **622**, 1202.

Chertok, I. M., and Grechnev, V. V.: 2003a, *Astron. Reports* **47**(2), 139.

Chertok, I. M., and Grechnev, V. V.: 2003b, *Astron. Reports* **47**(11), 934.

Chertok, I. M., and Grechnev, V. V.: 2005a, In K. P. Dere, J. Wang, and Y. Yan, editors, Coronal and Stellar Mass Ejections, *Proc. IAU Symp. 226, 2004*, 167.

Chertok, I. M., and Grechnev, V. V.: 2005b, *Solar Phys.* **229**, 95.

Covington, A. E. and Dodson, H. W.: 1953, *J. R. A. S. Canada* **47**, 207.

Delaboudinière, J.-P., Artzner, G. E., Brunaud, J. *et al.*: 1995, *Solar Phys.* **162**, 291.

Delaboudinière, J.-P., 2005, In K. P. Dere, J. Wang, and Y. Yan, editors, Coronal and Stellar Mass Ejections, *Proc. IAU Symp. 226, 2004*, 178.

Delannée, C., and Aulanier, G.: 1999, *Solar Phys.* **190**, 107.

Dere, K. P., Brueckner, G. E., Howard, R. A., *et al.*: 1997, *Solar Phys.* **175**, 601.

Dulk, G. A.: 1985, *Ann. Rev. Astron. Astrophys.* **23**, 169.

Gary, G. A.: 2001, *Solar Phys.* **203**, 71.

Gilbert, H. R., Holzer, T. E., Thompson, B. J., and Burkepile, J.T.: 2004a, *Astrophys. J.* **607**, 540.

Gilbert, H. R., and Holzer, T. E.: 2004b, *Astrophys. J.* **610**, 572.

Gilbert, H. R., Daou, A., Young, D., Detoma, G., and Tripathi, D. 2007, *Astrophys. J.*, submitted.

Grechnev, V. V., Chertok, I. M., Slemzin, V.A. *et al.*: 2005, *J. Geophys. Res.* **110**, A09S07.

Handy, B. N., Acton, L. W., Kankelborg, C. C. *et al.*: 1999, *Solar Phys.* **187**, 229.
Hansen, J. F., Tripathi, S. K. P., and Bellan, P. M.: 2004, *Phys. Plasmas*, **11**(6), 3177.
Harra, L. K., and Sterling, A. C.: 2001, *Astrophys. J.* **561**, L215.
Hudson, H. S., and Warmuth, A.: 2004, *Astrophys. J.* **614**, L85.
Hudson, H. S., and Webb, D. F.: 1997, *AGU Geophysical Monograph Ser.* **99**, 27.
Low, B. C.: 1982, *Astrophys. J.* **254**, 796.
Low, B. C.: 1984a, *Astrophys. J.* **281**, 381.
Low, B. C.: 1984b, *Astrophys. J.* **281**, 392.
Maksimov, V. P., and Nefedyev, V. P.: 1991, *Solar Phys.* **136**, 335.
Moreton, G. E.: 1960, *Astron. J.* **65**, 494.
Nakajima H., Sekiguchi H., Sawa M. *et al.*: 1985, *Publ. Astron. Soc. Japan* **37**, 163.
Nakajima, H., Nishio, M., Enome, S. *et al.*: 1994, *Proc. IEEE*, **82**, 705.
Newkirk, G. A.: 1961, *Astrophys. J.* **133**, 983.
Pohjolainen, S., Hori, K., and Sakurai, T.: 2007, *Solar Phys.*, submitted.
Sawier, C.: 1977, *Solar Phys.* **51**, 203.
Sedov, L. I.: 1981, Similarity methods and dimensional analysis in mechanics ($9^{\rm th}$ ed.), Moscow, Nauka, 448 pp. (in Russian).
Slemzin, V., Chertok, I., Grechnev, V. *et al.*: 2004, In A.V. Stepanov, E.E. Benevolenskaya, and A.G. Kosovichev, editors, Multi-Wavelength Investigations of Solar Activity, *Proc. IAU Symp. 223, 2004*, 533.
Slemzin, V. A., Grechnev, V. V., and Kuzin, S. V.: 2006, In 'Solar Activity and its Magnetic Origin', *Proc. IAU Symp. 233*, Cairo, Egypt, 361.
Slemzin, V., Kuzin, S., and Bogachev, S.: 2005, In D. Danesy, S. Poedts, A. De Groof, and J. Andries, editors, The Dynamic Sun: Challenges for Theory and Observations, *Proc. 11th European Solar Phys. Meeting*, ESA SP-600, 166.
Torii C., Tsukiji Y., Kobayashi S. *et al.*: 1979, *Proc. Res. Inst. Atm. Nagoya Univ.* **26**, 129.
Uchida, Y.: 1968, *Solar Phys.* **4**, 30.
Uralov, A. M., Lesovoi, S. V., Zandanov, V. G., and Grechnev, V. V.: 2002, *Solar Phys.* **208**, 69.
Uralov, A. M., Grechnev, V. V., and Hudson, H. S.: 2005, *J. Geophys. Res.* **110**, A05104.
Vršnak, B., Warmuth, A., Brajša, R., and Hanslmeier, A.: 2002, *Astron. Astrophys.* **394**, 299.
Warmuth, A., Vršnak, B., Aurass, H., and Hanslmeier, A.: 2001, *Astrophys. J.* **560**, L105.
Warmuth, A., Vršnak, B., Magdalenić, J., Hanslmeier, A., and Otruba, W.: 2004a, *Astron. Astrophys.* **418**, 1101.
Warmuth, A., Vršnak, B., Magdalenić, J., Hanslmeier, A., and Otruba, W.: 2004b, *Astron. Astrophys.* **418**, 1117.
Warmuth, A., Mann, G, and Aurass, H.: 2005, *Astrophys. J.* **626**, L121.
White, S. M., Thomas, R. J., and Schwartz, R. A.: 2005, *Solar Phys.* **227**, 231.
Yamaguchi, K., Sakurai, T., Irie, M. *et al.*: 2003, *Rep. Nat. Astron. Obs. Japan*, **6**(3–4), 101.
Zel'dovich, Ya. B., and Raizer, Yu. P.: 1966 Physics of shock waves and high-temperature hydrodynamic phenomena ($2^{\rm nd}$ ed.), Moscow, Nauka, 686 pp. (in Russian).
Zhang, Y., Wang, J., Attrill, G. D. R., Harra, L. K., Yang, Z., and He, X.: 2007, *Solar Phys.* **241**, 329.
Zhitnik, I. A., Bougaenko, O. I., Delaboudinière, J.-P. *et al.*: 2002, *Proc. 10th European Solar Physics Meeting, Prague (ESA SP-506)*, 915.
Zhukov, A. N., and Auchère, F.: 2004, *Astron. Astrophys.* **427**, 705.